AD-A105 184 FOREIGN TECHNOLOGY DIV WRIGHT-PATTERSON AFB OH F/G 20/4
ACTA MECHANICA SINICA (SELECTED ARTICLES).(U)
SEP 81
UNCLASSIFIED FTD-ID(RS)T-0704-81 NL

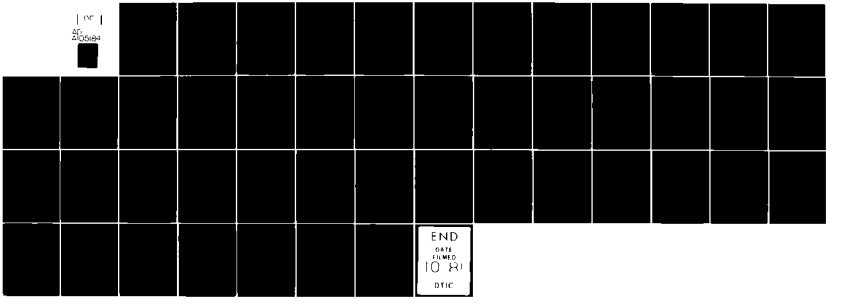

FTD-ID(RS)T-0704-81

FOREIGN TECHNOLOGY DIVISION

ACTA MECHANICA SINICA
(Selected Articles)

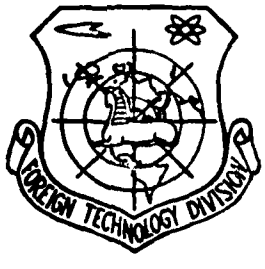

Approved for public release;
distribution unlimited.

EDITED TRANSLATION

(14) FTD-ID(RS)T-0704-81 (11) 11 September 1981

MICROFICHE NR: FTD-81-C-000839

(6) ACTA MECHANICA SINICA (Selected Articles)

English pages: 44

(24) Edited trans. of

Source: Acta Mechanica Sinica, Nr. 1, 1979, pp. 42-49, 70-73

Country of origin: (China) Nr 1 p42-49, 70-73 1979

Translated by: SCITRAN
F33657-78-D-0619

Requester: FTD/TQTA

Approved for public release; distribution unlimited.

THIS TRANSLATION IS A RENDITION OF THE ORIGINAL FOREIGN TEXT WITHOUT ANY ANALYTICAL OR EDITORIAL COMMENT. STATEMENTS OR THEORIES ADVOCATED OR IMPLIED ARE THOSE OF THE SOURCE AND DO NOT NECESSARILY REFLECT THE POSITION OR OPINION OF THE FOREIGN TECHNOLOGY DIVISION.	PREPARED BY: TRANSLATION DIVISION FOREIGN TECHNOLOGY DIVISION WP-AFB, OHIO.

242600 slr

TABLE OF CONTENTS

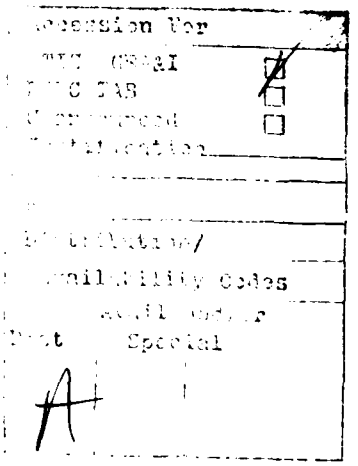

The Arbitrary Quasi-Orthogonal Surface Method for Computing Three-Dimensional Flow in Turbine Machinery*

II. Calculation of the Three-Dimensional Flow With the S_1-surface Twisted

Xin Xiao-Kang Jiang Jin-liang Zhu Shi-can
(Fudan University)

Abstract

On the basis of the quasi-orthogonal surface method, this paper obtains a three-dimensional flow field solution of inviscous fluids in turbine machinery. This method, under the condition allowed by the storage of the computer, can calculate any shapes of S_1 and S_2 surfaces (including twisting S_1 - surfaces) and obtain the shapes of space streamlines and the three-dimensional distribution of parameters such as velocity. The calculations for the two conditions of a centrifugal compressor with a small impeller (ϕ110) indicate the relative value of the twist of the S_1-surface is about 3 - 10%. The S_1-surface shows a double twist like a twist drill from the inlet to the outlet.

Under the assumptions that the fluid is incompressible, inviscous, and absolutely non-rotational, Reference [2] used a binary solution superposition method to calculate the results with twisted S_1 and S_2 surfaces. But because the turbine was not real, the results can only be used as a qualitative reference. On the basis of quasi-orthogonal surface method, this paper eliminates the assumption that the S_1 surface is a revolving body. In the processes of integration and the interpolation

*Received on November 18, 1977.

by equal difference of flux, an equi-parameter transformation is introduced to transform the flow region on the equi-orthogonal surfaces to a rectangular region on the (ξ, η) plane. It is then possible to use the procedures listed in Reference [1] and various modification procedures to obtain the iterative solution of the entire three-dimensional flow field. In the search for the reverse transformation of the equi-parameter transformation, this paper simultaneously offers three numerical methods (see Section III). The numerical calculation indicates that the accuracy is very good in the reverse transformation using a straight line quadrangle instead of the curved quadrangle. It is an approximation method which drastically reduces the calculation time. Using this method a computer program has been compiled for a centrifugal turbine and a calculation has been carried out on the modified centrifugal compressor turbine of the GJ11# pressure riser of Shanghai Diesel Engine Factory. The calculated results indicate the twist of the S_1 surface is relatively small. Therefore, it frequently uses the S_1 surface to carry out the calculation for the revolving body assumption as a fairly good approximation. The S_1 surface, in addition, shows a double twists like a twist drill from the inlet to the outlet. This method, in principle, is applicable to any type of turbines. However, for axial flow machinery we must add inlet and outlet corrections. The work in this area is currently in progress.

I. Basic Assumption and Solution to the Velocity Gradient Equation

This paper uses two basic assumptions: 1. The working medium (or fluid) isan inviscous, equi-C_p, and equi-C_v perfect gas. The flow may be unisoentropic. However, for ease of description, the entropy gradient term is neglected from the equation. The friction loss of the real gases is reflected by

the variation process same as the one used in Reference [1].

2. The flow passing through the turbine is a constant relative to the turbine. The kinetic equations are written in a relative cylindrical coordinate system (r, θ, z) .

The basic equations used in this work still are equations (1) and (2) in Reference [1]. Here we slightly modify these equations and rewrite them as

$$\frac{dW}{dq} = AW + B + \frac{1}{W}\left(\frac{dh'_0}{dq} - \omega \frac{d\lambda}{dq}\right) \tag{1}$$

where

$$\left.\begin{aligned} A &= \frac{\cos^2\beta\left(\cos\alpha \dfrac{dr}{dq} - \sin\alpha \dfrac{dz}{dq}\right)}{r_c} - \frac{\sin^2\beta \dfrac{dr}{dq}}{r} + \sin\alpha \sin\beta \cos\beta \frac{d\theta}{dq} \\ B &= \left(\frac{dr}{dq}\sin\alpha + \frac{dz}{dq}\cos\alpha\right)\cos\beta \frac{dW_m}{dm} - 2\omega \sin\beta \frac{dr}{dq} \\ &\quad + r\cos\beta\left(\frac{dW_\theta}{dm} + 2\omega \sin\alpha\right)\frac{d\theta}{dq} \end{aligned}\right\} \tag{2}$$

On the quasi-orthogonal surfaces, two independent variables q_m and θ are introduced as in Reference [1]. Therefore, in the quqsi-orthogonal surface of the single blade channel on the (θ, q_m) plane (it is the region between the pressure surface of one blade to the suction surface of another blade) the flow field is shown approximately in Figure 1. The intersection between S_2 surface and the quasi-orthogonal surface is indicated as the dotted line. The intersection of the S_1 surface and the quasi-orthogonal surface is shown as the point-solid line. If the problem we are solving has N + 1 S_1 surfaces and H + 1 S_2 surfaces, then the equations of the intersection between the quasi-orthogonal surfaces and the S_2 surfaces can be written as

$$\theta = f_k(q_m) \quad (k = 1, 2, \cdots, H + 1) \tag{3}$$

The intersection equations of the quasi-orthogonal surfaces and the S_1 surfaces can be written as

$$q_m = g_j(\theta) \quad (j = 1, 2, \cdots, N+1) \tag{4}$$

Obviously, when $g_j(\theta)$ = const, it is the situation that S_1 surface is a revolving surface.

The first few steps of the problem solving procedure used in this paper are similar to those used in Reference [1]. Steps 1 - 5 are basically identical to those in Reference [1]. The only thing is that the coordinates (r_p, θ_p, z_p) of an arbitrary lattice point p (it is the intersecting point between S_1 surfaces, S_2 surfaces and the quasi-orthogonal surfaces) on the streamline should be a three-dimensional numerical set and it is no longer a two dimensional numerical set as in Reference [1]. Similarly, α, β, r_c , etc. are also presently a three-dimensional numerical set.

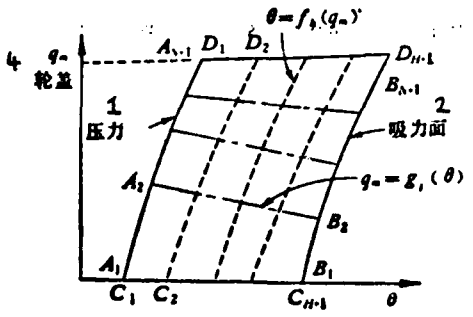

Figure 1. Key: 1. Pressure, 2. Suction surface, 4. Rotating cover.

With respect to setp 6 in Reference [1], we carry out the following modification. In order to make point p or the streamline satisfy equation (1) simultaneously in both the q_m and the

θ directions, the following modification is made in solving for the velocity gradient equation as proposed in Reference [1]. Assuming that the value W at point A in Figure 2 is known, then we first proceed with a numerical liner integration along AB to find out the W value of all the points along AB. We further perform integration along the intersecting line with the S_1 surface to obtain the W value at all the lattice points (Figure 2a). We shall designate them as the $W_1[j,k]$ numerical set. On the other hand, let us start from point A to integrate linearly along AC in order to obtain the W value of all points along AC and then integrate along the intersecting line with the S_2 surface. The obtained W values at all thelattice points are designted as the $W_2[j,k]$ numerical set. Finally, let

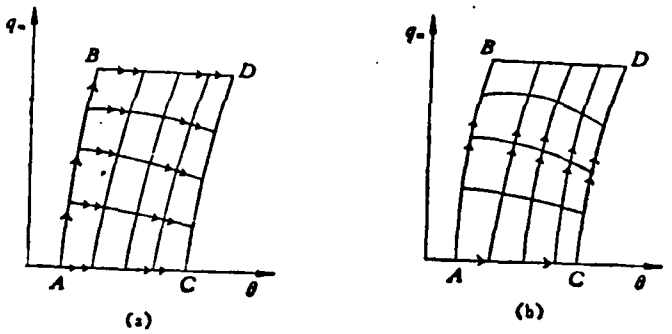

Figure 2

us take

$$W[j,k] = \frac{W_1[j,k] + W_2[j,k]}{2} \quad \begin{pmatrix} j = 1, 2, \cdots, N+1 \\ k = 1, 2, \cdots, H+1 \end{pmatrix}$$

as the relative velocity values of all the lattice points on the quasi-orthogonal surfaces. The mathematical meaning of this process is to make any point P simultaneously satisfy equation (1) in two directions under the "average" idea described above. In addition, we also use the numerical method which starts from the center of the flow field toward the perimeter

to seek for solution. In this method the original starting point A is moved to the center of the flow field E (Figure 3). This would further raise the accuracy of the numerical solution.

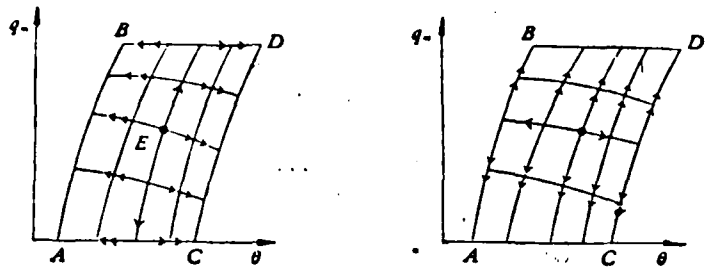

Figure 3

II. Flux Integration and Equi-Parameter Transformation

The major difficulty brought about by the elimination of the assumption that the S_1 surface is a revolving surface is how to carry out steps 8 and 9 used in Reference [1]. From Reference [1], it is known that the mass flux equation in the channel between two neighboring bladesthrough any quasi-orthogonal surface is

$$G = \iint_s \rho g W_m \cos(\psi - \alpha) r d\theta dq_m \qquad (5)$$

where the integration region 5 is the ABCD region on the quasi-orthogonal surface (Figure 2). Since the S_1 surface is not a solving surface, the integral of equation (5) can no longer be written as a quadratic integration (i.e. integration first with respect to θ and then to q_m) as in Reference [1]. It must be written as a double integral as in equation (5). However, there is certain difficulty in the direct integration as in equation (5). For that, we have to introduce an equi-parameter transformation which transforms the ABCD region on

the quasi-orthogonal surface into a rectangular region on a certain transformation plane - (ξ, η) plane and also simultaneously transform every curved quadrangles regions surrounded by the intersections of S_1 and S_2 surfaces into rectangular region. Thus, the regions on the (ξ, η) plane become very regular. The intersection line of the S_1 surface is transformed into the η = const straight line and the intersection line of the S_2 surface is transformed into the ξ = const straight line. Therefore, the integrations in equation (5) become much easier on the (ξ, η) plane.

The following is the derivation of the equi-parameter transformation equations. Let us assume that there is a region ABCD surrounded by a curved quadrangle (Figure 4a) and the equations for the four sides are assumed as:

$$\left.\begin{aligned} AC: q_m &= q_l(\theta), \quad BD: q_m = q_{l+1}(\theta) \\ AB: \theta &= f_k(q_m), \quad CD: \theta = f_{k+1}(q_m) \end{aligned}\right\} \tag{6}$$

We are seeking for a transformation which transforms the curved quadrangle ABCD into the rectangle A*B*C*D* on the (ξ, η) plane (Figure 4b) and make

$$\left.\begin{aligned} A^*C^*: \eta &= \eta_l, \quad B^*D^*: \eta = \eta_{l+1} \\ A^*B^*: \xi &= \xi_k, \quad C^*D^*: \xi = \xi_{k+1} \end{aligned}\right\} \tag{7}$$

We found that the equi-parameter transformation below can achieve the above objectives:

$$\left.\begin{aligned} \frac{\xi - \xi_k}{\xi_{k+1} - \xi_k} &= \frac{\theta - f_k(q_m)}{f_{k+1}(q_m) - f_k(q_m)}, \quad f_k(q_m) < \theta \leq f_{k+1}(q_m) \\ \frac{\eta - \eta_l}{\eta_{l+1} - \eta_l} &= \frac{q_m - g_l(\theta)}{g_{l+1}(\theta) - g_l(\theta)}, \quad g_l(\theta) < q_m \leq g_{l+1}(\theta) \end{aligned}\right\} \tag{8}$$

For convenience, we can simplify equation (θ) as

$$\xi = \xi(\theta, q_m), \quad \eta = \eta(\theta, q_m) \tag{9}$$

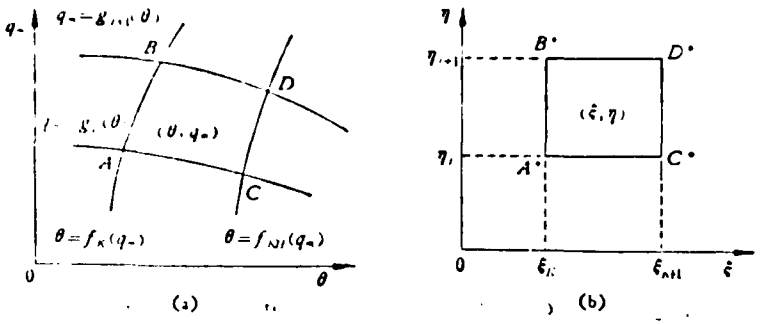

Figure 4

It is easy to write the Jacobi determinant which transforms equation (9) as

$$J = \frac{D(\xi, \eta)}{D(\theta, q_m)} = \begin{vmatrix} \frac{\partial \xi}{\partial \theta} & \frac{\partial \xi}{\partial q_m} \\ \frac{\partial \eta}{\partial \theta} & \frac{\partial \eta}{\partial q_m} \end{vmatrix} = \frac{\partial \xi}{\partial \theta}\frac{\partial \eta}{\partial q_m} - \frac{\partial \xi}{\partial q_m}\frac{\partial \eta}{\partial \theta} \tag{10}$$

Therefore, the flux integral (5) can be transformed into

$$G = \iint_s CK(\theta, q_m) d\theta dq_m = \iint_{s^*} CK(\xi, \eta) \frac{1}{|J|} d\xi d\eta \tag{11}$$

where

$$CK(\theta, q_m) = \rho g |V_m| \cos(\alpha - \psi) r.$$

If we take S* as a unit square area, then equation (11) can be written in the quadratic integral form:

$$G = \int_0^1 d\xi \int_0^1 CK(\xi, \eta) \frac{1}{|J|} d\eta = \int_0^1 d\eta \int_0^1 CK(\xi, \eta) \frac{1}{|J|} d\xi \tag{12}$$

Here the value of the Jacobi equation /J/ at the lattice point $(\theta_{i,k}, q_{m_i,k})$ is

$$\frac{1}{|J|} = \frac{[f_{k+1}(q_{m_i,k}) - \theta_{i,k}][g_{i+1}(\theta_{i,k}) - q_{m_i,k}]}{[1 - f_k'(q_{m_i,k}) \cdot g_i'(\theta_{i,k})]\,\Delta\xi\Delta\eta} \tag{13}$$

where $\Delta\xi = \xi_{i+1} - \xi_i = 1/H$, $\Delta\eta = \eta_{i+1} - \eta_i = 1/N$.

Using this quadratic numerical calculation, we can obtain the calculated flux value. In order not to treat the coordinates "specially", from now on in all our procedures we will use the "average" method as we did in solving the velocity gradient equation. For example, in determining the flux, we let

$$G_1 = \int_0^1 d\eta \int_0^1 CK(\xi, \eta)\frac{1}{|J|}d\xi \tag{14}$$

$$G_2 = \int_0^1 d\xi \int_0^1 CK(\xi, \eta)\frac{1}{|J|}d\eta \tag{15}$$

then the calculate flux

$$G = (G_1 + G_2)/2 \tag{16}$$

Compare G with the given fixed flux G_0, if $|G - G_0|/G_0 < \varepsilon_G$, then switch to step 8. Otherwise use the method similar to the one used in Reference [1] to correct the velocity value at point A or E and repeat steps 6 and 7.

III. Flux Interpolation by Equal Difference and the Reverse Transformation

For step 8, which is the step using the interpolation by equal difference method to obtain the new coordinate positions of the streamline, we carry it out on the (ξ, η) plane. Because the integral is the quadratic integral form, therefore we can proceed using the same method as in Reference [1]. First we

obtain a set of new streamline coordinates $(\xi_{G1}, \eta_{G1})_{i,k}$ from equation (4) and then we obtain another set of new streamline coordinates (ξ_{G2}, η_{G2}) from equation (15). After taking their average value, we get the new positions of the streamline coordinate points from the interpolation by equal difference in flux

$$\xi_G = (\xi_{G1} + \xi_{G2})/2, \quad \eta_G = (\eta_{G1} + \eta_{G2})/2 \tag{17}$$

The next problem is how to find θ_G and q_{mG} on the physical plane (from q_{mG} we can get r_G and z_G) once the new streamline coordinate positions ξ_G and η_G are found.

From the equi-parameter transformation (8), we know that it is pretty difficult to find θ_G and q_{mG} from ξ_G and η_G. It is because the real analytical solutions of $g_i(\theta)$ and $f_k(q_m)$ are actually not known. We have used various methods to look for the reverse transformation. Here we are only going to discuss and compare three methods which we have used to conduct detailed calculations.

1. Rigorous and "accurate" Reverse Transformation. From the equi-parameter transformation (8), we know that when $\xi_k < \xi_G \leqslant \xi_{k+1}$ and $\eta_i < \eta_G \leqslant \eta_{i+1}$

$$\left.\begin{aligned} \xi_G &= \frac{\xi_G - \xi_k}{\xi_{k+1} - \xi_k} = \frac{\theta - f_k(q_m)}{f_{k+1}(q_m) - f_k(q_m)} \\ \eta_G &= \frac{\eta_G - \eta_i}{\eta_{i+1} - \eta_i} = \frac{q_m - g_i(\theta)}{g_{i+1}(\theta) - g_i(\theta)} \end{aligned}\right\} \tag{18}$$

Our purpose is to locate the θ_G and q_{mG} which satisfy equation (18). For that, we are rewriting equation (18) as

$$\left.\begin{aligned} \theta &= f_k(q_m) + \xi_G[f_{k+1}(q_m) - f_k(q_m)] \\ q_m &= g_i(\theta) + \eta_G[g_{i+1}(\theta) - g_i(\theta)] \end{aligned}\right\} \tag{19}$$

If an initial value $q_m^{(0)}$ is given by an approximation method, then we can use the following iteration method to obtain the iterative values of θ and q_m:

$$\left.\begin{aligned} \theta^{(n)} &= f_k(q_m^{(n)}) + \xi_{ik}[f_{k+1}(q_m^{(n)}) - f_k(q_m^{(n)})] \\ q_m^{(n+1)} &= g_i(\theta^{(n)}) + \eta_{ik}[g_{i+1}(\theta^{(n)}) - g_i(\theta^{(n)})] \end{aligned}\right\} \qquad (20)$$

Iteration stops when $|q_m^{(n+1)} - q_m^{(n)}| < \varepsilon_0$. Thus the reverse transformation which is "accurate" in the sense of approximation in numerical value is obtained.

2. The Reverse Transformation Using the Linear Quadrangle Approximation.

Because it is time consuming to use the above equations, the reverse transformation which replaces the curved quadrangle by the linear quadrangle is proposed. It is obvious that, with increasing N and H, this approximation is very good.

Let us consider an arbitrary curved quadrangle ABCD (Figure 4) with the vertices

$$A(\theta_{i,k}, q_{mi,k}), \quad B(\theta_{i+1,k}, q_{mi+1,k})$$
$$C(\theta_{i,k+1}, q_{mi,k+1}), \quad D(\theta_{i+1,k+1}, q_{mi+1,k+1})$$

The reverse transformation equations using the linear quadrangle approximation can be obtained through very simple mathematical operations as

$$\left.\begin{aligned} \theta &= \frac{b\xi - a + (c\xi + K_{ij,k})(e\eta - d)}{1 - (c\xi + K_{ij,k})(f\eta + K_{i,k})} = \theta(\xi, \eta) \\ q_m &= \frac{e\eta - d + (f\eta + K_{i,k})(b\xi - a)}{1 - (c\xi + K_{ij,k})(f\eta + K_{i,k})} = q_m(\xi, \eta) \end{aligned}\right\} \qquad (21)$$

where

$$
\left.
\begin{aligned}
&a = K_{ij,k}q_{mj,k} - \theta_{i,k}, \quad b = \Delta\theta + K_{ij,k}q_{mj,k} - K_{ij,k+1}q_{mj,k+1} \\
&c = -K_{ij,k} + K_{ij,k+1}, \quad d = K_{i,k}\theta_{i,k} - q_{mj,k} \\
&e = \Delta q_m + K_{i,k}\theta_{i,k} - K_{i+1,k}\theta_{i+1,k}, \quad f = K_{i+1,k} - K_{i,k} \\
&\Delta\theta = \theta_{i,k+1} - \theta_{i,k}, \quad \Delta q_m = q_{mj+1,k} - q_{mj,k} \\
&K_{i,k} = \frac{q_{mj,k+1} - q_{mj,k}}{\theta_{i,k+1} - \theta_{i,k}}, \quad K_{i+1,k} = \frac{q_{mj+1,k+1} - q_{mj+1,k}}{\theta_{i+1,k+1} - \theta_{i+1,k}} \\
&K_{ij,k} = \frac{\theta_{i+1,k} - \theta_{i,k}}{q_{mj+1,k} - q_{mj,k}}, \quad K_{ij,k+1} = \frac{\theta_{i+1,k+1} - \theta_{i,k+1}}{q_{mj+1,k+1} - q_{mj,k+1}}
\end{aligned}
\right\} \qquad (22)
$$

Thus, after ξ_G and η_G are known, we can use equation (21) to directly obtain θ_G and q_{mG}. The results of numerical calculation (shown later) indicate that this method almost has the same precision as the "accurate" reverse transformation. However, the calculation time can be drastically reduced. It is even possible to reduce the computation time by 1/3.

3. Simplified Uni-directional Sampling Approximation

In our earlier computation process, we have used another simple approximation method which considers the reverse transformation approximately as

$$\theta = \theta(\xi), \quad q_m = q_m(\eta) \qquad (24)$$

Therefore, we can use the uni-direction sample strip interpolation method to obtain the values of $\theta_{Gi,k}$ and $q_{mG,j,k}$ from $(\xi_{Gi,k}, \eta_{G,j,k})$. This approximation method is very simple but its accuracy is relatively poor.

After the reverse transformation is obtained, we can proceed with the same steps which follow as in Reference [1]. The iteration continues with the maximum momentum variation max at the new streamline point is less than the given accuracy ε_{max}. The actual details of program compilation are omitted here.

IV. Calculated Examples and Analysis

We have used the above method to compile the 719 computer program of our school and carried out an numerical calculation on the modified centrifugal compressor turbine of the GJ11# pressure riser of Shanghai Diesel Engine Factory. The calculation regime is: inlet temperature T_1 = 293°K, inlet specific gravity $\gamma_1 = 1.1695 kg/m^3$, isobaric specific heat $C_p = 1022.33 kg \cdot m/kg \cdot °K$, variational coefficient n_o = 1.506, mass flux C_o = 0.3 kg/s, angular velocity $\omega = 4188.8 rad/s$, number of blades Z_N = 14, number of quasi-orthogonal surfaces m = 13, number of S_1 surfaces N + 1 = 9, number of S_2 surfaces H + 1 = 9.

Since the calculated data are too much to show, we are only going to present part of the data showing the major relevant results. Figure 5 shows the meridional surface lines of the turbine and the meridional line of the S_2 surfaces. Figure 6 gives the distribution of relative Mach number on the average S_2 surface ($k = 5$) and also shows the comparison of the distribution of M using the revolving surface assumption with our results when $k = 5, j = 1, 5, 9$ (notice that the $\bar{m}$ coordinate in the figure, one uses the percentage of the arc length of the meridional streamline and the other uses the percentage of the arc length of spatial streamline). Figures 7 - 9 show the distribution of M and the diagrams of streamline of the cross blade spatial streamlines when j = 1, 5, 9. Figure 10 indicates the twisting condition of the intersection between the quasi-orthogonal surfaces S_1 and S_2 when i = 1, 5, 9, 13. It also simultaneously gives a comparison between of the results of calculation obtained using the revolving surface assumption at the inlet surface (i = 1) and those using the method described in this paper. It only shows the deviation of the S_1 surfaces. Figure 11 shows the comparison of results obtained using the three reverse transformation methods on the calculation of the

twisting of the S_1 surfaces (only i = 1 is plotted). Figure 12 shows the condition of S_1 surface twisting when the number of blades Z_N = 18.

From these calculated examples, we can see the following:

1. From Figures 6 - 9, it was found that the results obtained using the method in this paper is basically similar to those obtained using the method described in Reference [1]. From Figures 10 and 12, it was found that the relative twisting of the surfaces is relatively small, approximately 3 - 10%. Therefore, the results obtained using the revolving surface assumption and non-revolving surface method are very close. Therefore, in general, the revolving surface assumption is still applicable.

2. From Figure 10, we can see that the present calculated shapes of the S_1 surfaces sometimes appear to be slightly convex (the surface of J = 3 is most apparent). The height at both ends varies with i - 1, 5, 9, 13 differently. At the inlet (i = 1) the pressure surface q_m is higher than the suction surface. This phenomenon is consistent with the results obtained from the two-dimensional simplification of the axi-symmetrical flow machinery. At the front middle part of the centrifugal turbine (i = 5), the S_1 surface still shows the phenomenon of being slightly convex. The interseting point q_m on the pressure surface, however, is lower than that on the suction surface. Therefore, the surface shows a reverse buckling (twisting) phenomenon. Further back, at i = 9, 13 (outlet), another reverse twisting effect appears which causes that the q_m on the pressure surface to behigher than that on the suction surface on the S_1 surface. This phenomenon is not consistent with the result obtained in the two-dimensional simplified calculation of the axial flow machinery. As for whether this belongs to the special

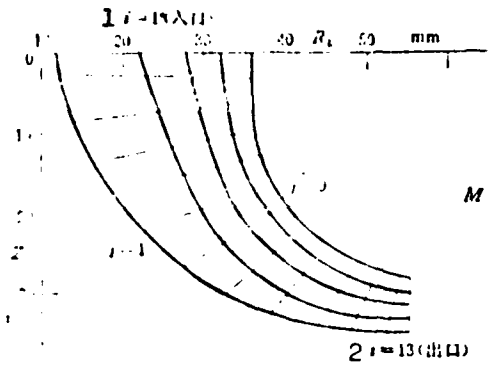

Figure 5. Key: 1. inlet 2. outlet

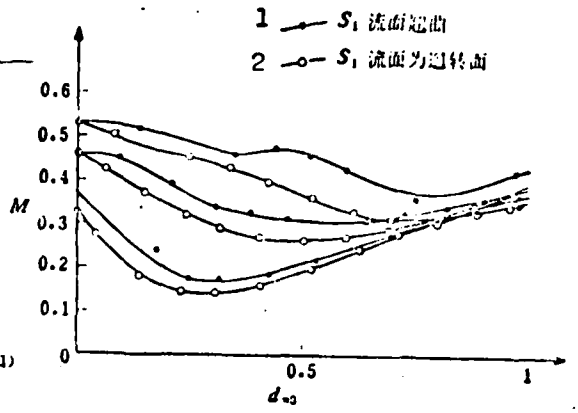

Figure 6. Key: 1. S_1 surface twisted, 2. S_1 surface is a revolving surface.

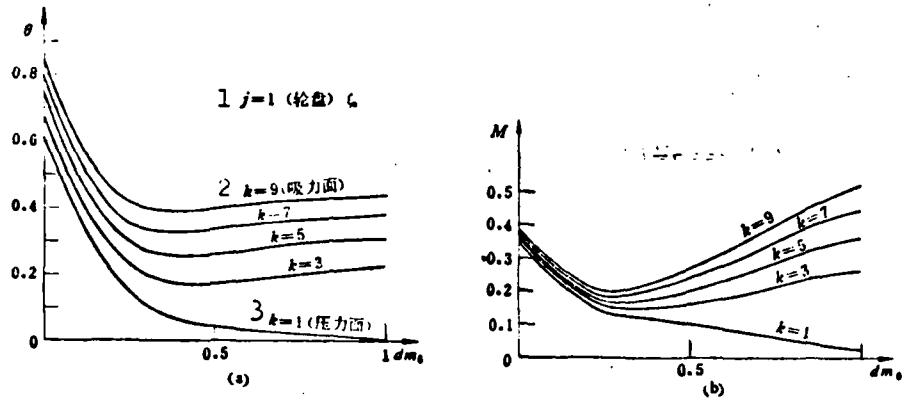

Figure 7

Key: 1. j = 1 rotating disc, 2. k = 9 suction surface, 3. k = 1 pressure surface

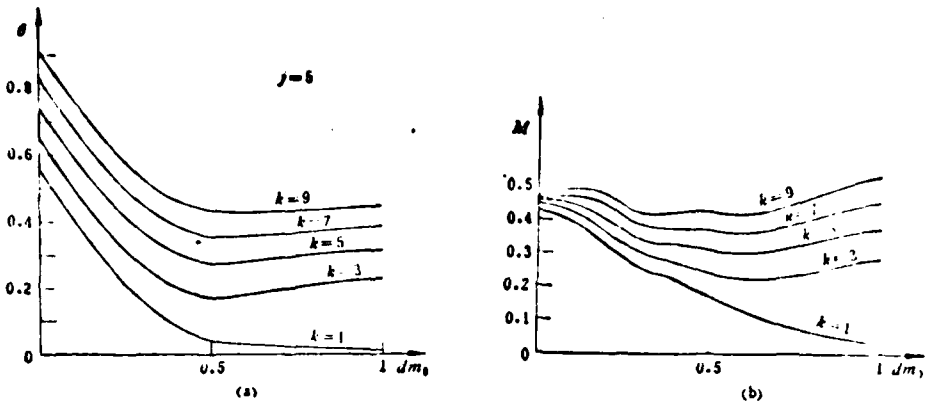

Figure 8

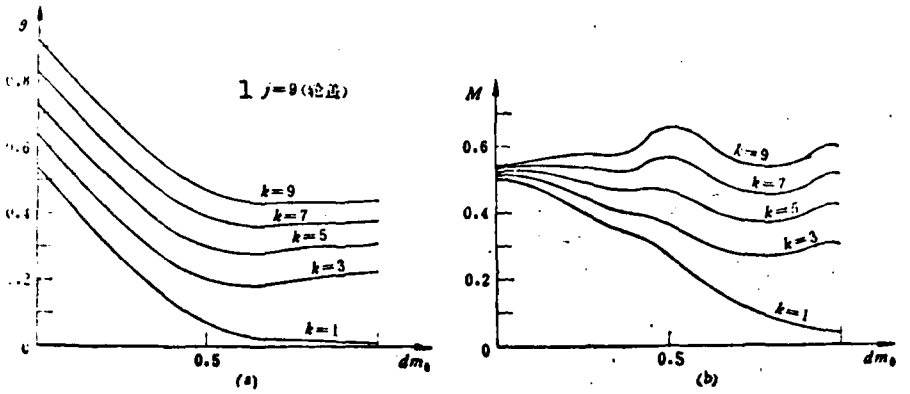

Figure 9.
Key: 1. j = 9 rotating cover

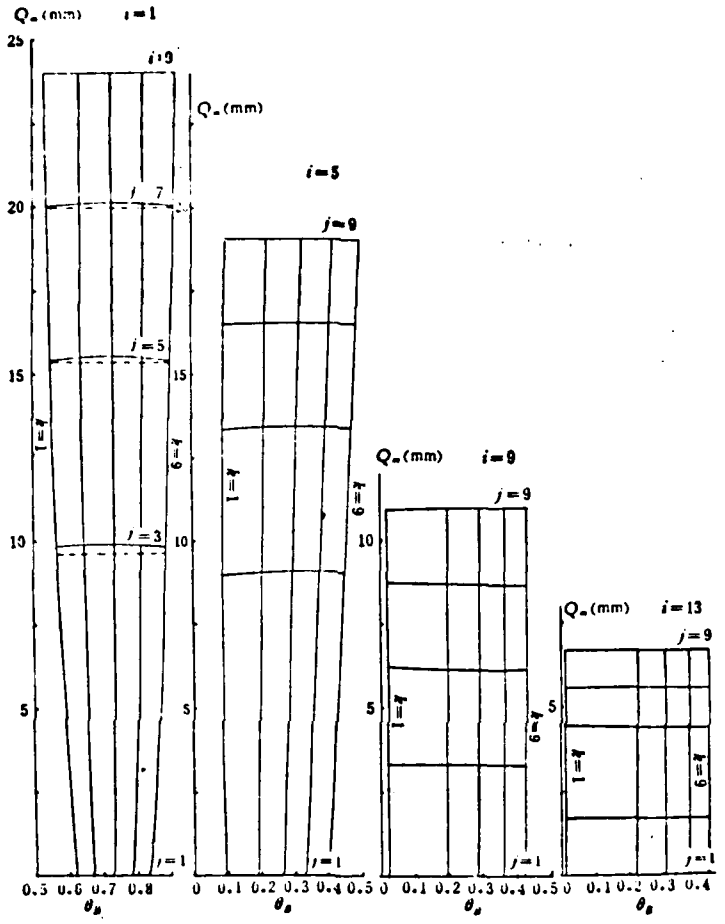

Figure 10

Key: 1. ----- is the result obtained using the assumption that S_1 surface is a revolving surface

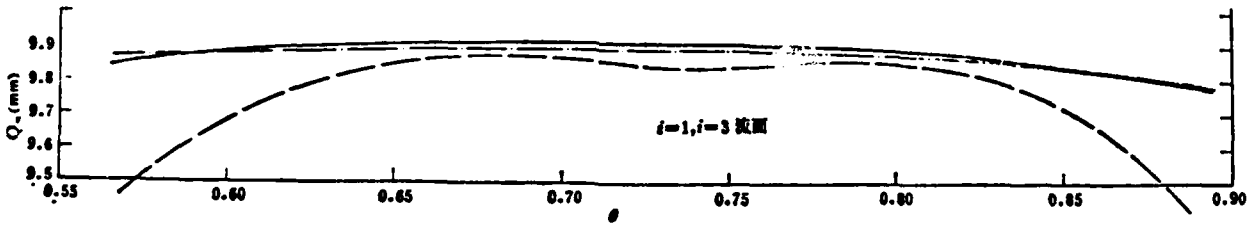

Figure 11

Key: 1. i=1, i=3 surface

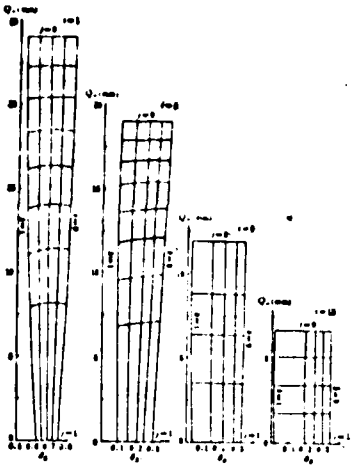

Figure 12

characteristics of the centrifugal machinery, it is still yet to be verified.

3. From Figure 11, it was found that the linear quadrangle approximation seems to have the same accuracy as the "accurate" iterative reverse transformation method. The relative errors is about 0.5%. The advantage of the linear quadrangle approximation method is the reduction of calculation time by 1/3. For example, when the convergence accuracy ϵ_{max} = 1 mm, both methods require 16 iterations while the calculation time can be reduced from 138 to 93 minutes. Therefore, the use of the linear quadrangle approximation is reliable and time saving. The use of uni-directional sampling approximation has a larger error. The maximum relative error is about 2%.

4. Figure 12 shows the calculated results when max < 10^{-5}m. At this time the maximum momentum variation of Mach number is 3 x 10^{-4}. This can be considered to be convergent. But the calculation time is too long.

V. Conclusions

This paper uses an equi-parameter transformation to further develop the procedures mentioned in Reference [1] in order to calculate the three dimensional flow field in the blade channel for an inviscous fluid. The condition of twisting of the S_1 and S_2 surfaces can also be quantitatively determined simultaneously. Based on the results from one turbine, it is reliable. But due to the lack of experimental data and analytic solutions, there is no way to reach certain conclusions for some phenomena and results (such as the small degree of twisting of the surfaces, the double twisting phenomenon, etc.) and it still requires further computational and experimental verifications.

References

[1] Chi Sho Kang and Chiang Chin Lian, Mechanics, 2, (1977).

[2] Stanitz, J. D. & Ellis, G. O., Flow Surfaces in Rotating Axial-Flow Passages, NACA TN-2834 (1952).

[3] Wu, C. H. (吳仲華) , A General Theory of Three-Dimensional Flow in Subsonic and Supersonic Turbomachines of Axial, Radial and Mixed Flow Types, NACA TN-2604 (1952).

THE PRINCIPLES AND METHODS FOR SHAPING THE WING ROOT REGIONS OF A WING-BODY COMBINATION AT TRANSONIC AND LOWER SUPERSONIC SPEEDS*

Yang Tso Sheng, Tai Chia Tsun, Ch'en Ching Sung, Fan Chia I
(Nanching Aeronautical Institute)

Abstract

On the basis of the author's previous work[1], this paper deals with the principles and methods for the combined shaping of the wing root regions of a wing-body combination, in accordance with the requirements of area rule and shockless pressure field.

It is shown that the favorable non-midwing arrangement is able to reduce the amount of fuselage sha ng required for the reduction of the zero lift wave drag of a wing-body combination. The combined shaping so designed may thus be realized more easily in structual arrangement.

I. INTRODUCTION

In fuselage designs based on the "area rule", there usually still exists the problem of the appearance of shock waves on the wings and the reduction of wave drag to the expected value cannot be achieved. If one requires that the fuselage shaping be such that when the pressure field of the fuselage is added to that of the isolated wing, the resultant pressure distribution in the wing root regions will be congruent with the pressure distribution on the equivalent yawed wing, then shock waves will definitely not appear on the wings. In this manner, the "area rule" can be used to full advantage [1-3]. The fuselage shaping required when such a pressure field method is adopted is generally fairly large. In order to reduce the amount of shaping, one needs to resort to combined shaping, i.e., the wing shape in the wing root regions needs to be appropriately tailored--the wing thickness near the front of

*Received February 11, 1974

the wing root regions has to be increased and the position of maximum wing thickness has to be shifted gradually from outside of the wing root regions towards the wing root regions [4]. In addition, we have found that if a favorable non-midwing arrangement is adopted, fuselage shaping can be substantially reduced. We have given in reference [5] the method for calculating the pressure field of the fuselage for a non-midwing arrangement. The equation derived there will be directly applied in the present paper.

2. THE AERODYNAMIC DESIGN OF THE WING SECTION AND FILLET IN THE WING ROOT REGIONS

For a given Mach number M in supersonic designs, the wing section at the wing root for a given pressure distribution can only be obtained by means of successive approximations. Such a procedure is tedious. The key to achieving faster convergence lies in choosing correctly the wing section in the wing root regions in the first approximation.

1. Determination of wing section in the wing root regions in the first approximation

We simplify the problem by considering an infinite swept-back wing of constant chord. The sweep angle Λ is equal to the sweep-back of the minimum pressure isobar of the equivalent yawed wing. The relation between the linearized pressure coefficient C_p of the infinite swept-back wing under the conditions of subsonic leading edge and the slope dz/dx of the wing section has been given in [6] to be

$$C_p = -\left\{\left[\frac{2\cos\Lambda}{\pi\sqrt{1-M^2\cos^2\Lambda}}\ln\left[\frac{\sqrt{1-M^2\cos^2\Lambda}+\sin\Lambda}{\sqrt{1-M^2\cos^2\Lambda}-\sin\Lambda}\right]\right\}\frac{dz}{dx}\right. \tag{1}$$

There are definite difficulties associated with solving for the shape of the wing section by means of Equation (1) under given pressure distribution on the equivalent infinite yawed wing. This is because for subsonic critical flow, the C_p near the trailing edge of the equivalent infinite yawed wing has to return to a positive value. According to Equation (1), the slope of the wing section should be positive. This causes the wing section to stay open along the trailing edge. Note that in subsonic flow round infinite swept-back wing of constant chord, the pressure distribution on the wing section in the root regions is given by [7,8].

$$C_p = \frac{-2\cos\Lambda}{\sqrt{1-M^2\cos^2\Lambda}}\left\{\frac{1}{\pi}\int_0^1 \frac{\frac{dz}{dx}\,dx'}{x-x'} - \frac{1}{\pi}\ln\left[\frac{\sqrt{1-M^2\cos^2\Lambda}+\sin\Lambda}{\sqrt{1-M^2\cos^2\Lambda}-\sin\Lambda}\right]\frac{dz}{dx}\right\} \qquad (2)$$

Comparing Equations (1) and (2), one sees that the second term in Equation (2) is nothing but the pressure coefficient of the wing section in the root region under conditions of supersonic flow round an object (the leading edge of subsonic flow). Its weight in Equation (2) increases with the M number of the oncoming flow. Hence, we make the pressure distribution under higher subsonic M numbers (e.g., M = 0.9) equal to that of the corresponding equivalent infinite yawed wing in accordance with Equation (2). The wing section in the root regions thus determined not only results in improved pressure distribution on the wing section in the root region under transonic flows, but also causes the pressure distribution of the wing section in the root region to converge to that of its corresponding infinite yawed wing under lower supersonic flows. Therefore, it is reasonable to use this as a first approximation to the shape of the wing section in the root region for a given M number in supersonic designs. We express the integral and dz/dx in Equation (2) in terms of sums of the ordinate z of the wing section:

$$C_p(x_\nu) = -\frac{2\cos\Lambda}{\sqrt{1-M^2\cos^2\Lambda}}\left[\sum_{\mu=1}^{N-1} s_{\nu\mu}^{(1)} z_\mu - f(\Lambda)\sum_{\mu=1}^{N-1} s_{\nu\mu}^{(2)} z_\mu\right] \qquad (3)$$

In which

$$f(\Lambda) = \frac{1}{\pi}\ln\left|\frac{\sqrt{1-M^2\cos^2\Lambda}+\sin\Lambda}{\sqrt{1-M^2\cos^2\Lambda}-\sin\Lambda}\right| \qquad (\nu = 1, 2, \cdots, N-1) \qquad (4)$$

Thus, for a given pressure distribution on the wing root wing section, one can solve from Equation (3) the ordinate z_μ corresponding to any specific x_μ. Here, x_μ and z_μ are dimensionless quantities. The characteristic length used for conversion into dimensionless quantities is the wing root chord c_o. In this set of equations, N is the number of terms in the sums. Value for x_ν, $s_{\nu\mu}^{(1)}$ and $s_{\nu\mu}^{(2)}$ corresponding to x_ν in the cases N = 8,16,32 have been tabulated [7]. Suppose the variation in the wing root wing section will converge at spanwise position Y_2. Take the wing section at that point to be the control wing section. The region between the wing root wing section and the control wing section is called the wing root region. The spanwise variation of the wing section in the wing root region at each point on the lines of constant percentage chord can be regarded as a parabola or a cosine curve. As the entire wing region within the front Mach line of the wing section in the root regions has some effect on the pressure distribution on the wing section in the root regions, one can take the spanwise coordinate of the point of intersection of the said front Mach line and the leading edge of the wing to be Y_2.

Results of calculations for actual examples show that if one makes the pressure distribution on the wing root coincide exactly with that on the equivalent yawed wing, negative values for the ordinate of the wing root wing section will appear near the trailing edge. This means that the upper and lower surfaces of the wing section will meet at some point in front of the trailing edge and not close to the trailing edge. This is not reasonable. Hence, one can only match the pressure distribution on the wing root wing

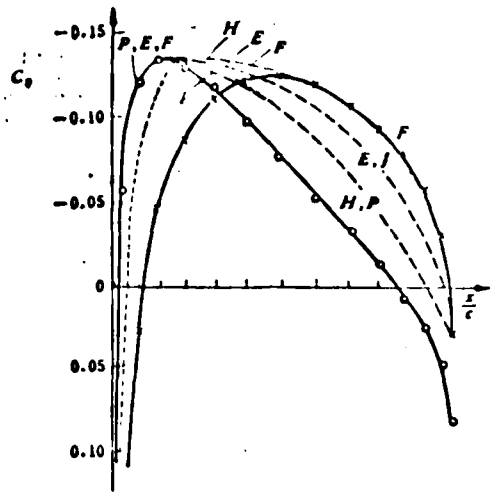

Figure 1. Chordwise distribution of C_p of wing root wing section
o equivalent yawed wing
x original wing root wing section

section to that on the equivalent yawed wing to the largest possible extent. Our procedure is as follows: 1) Modify the pressure distribution before the minimum pressure point of the original wing root wing section so that it coincides exactly with that on the equivalent yawed wing. The pressure distribution after the minimum pressure point should be between the pressure distributions of the equivalent yawed wing and the original wing root wing section, as illustated by curves P, E, F in Figure 1. 2) Make the pressure distribution before and after the minimum pressure point lie between those of the equivalent yawed wing and the original wing root wing section, as illustrated by curves H and J in Figure 1. Under the requirement that the trailing edge of the wing section should be closed, the closer the pressure distribution on the wing root wing section is to that on the equivalent yawed wing, the further forward will the point of maximum thickness of the wing root wing section shift. This causes the entire wing section to reduce in thickness. To overcome this problem, we note that the point of maximum thickness shifting forward means that the thickness at the leading edge of the wing

section in the root regions needs to be increased. Hence, we can satisfy this requirement without having to move the point of maximum thickness of wing section excessively forward by extending the chord of the wing section in the root regions, i.e., by adding a fillet to the wing root region.

2. The aerodynamic design of the wing root region fillet in the first approximation

Consider a trapezoidal swept-back wing. Suppse the position of the point of minimum pressure on the first approximation wing root wing section has already been shifted from point C on the original wing root wing section to point B. Since point B still falls behind the point of minimum pressure A of the equivalent yawed wing (Figure 2), one needs to employ the method of lengthening the chord of wing root to make the point of minimum pressure of the wing root wing section fall on point A. Let the distance between point B and the leading edge be OB, and denote its ratio to the original chord OD as x_1, i.e., $x_1 = OB/OD$. If the chord of the wing root wing section is extended to O' such that the point of miminum pressure falls on point A, then since $x_1 = \frac{O'A}{O'D} = \frac{OB}{OD}$ and $OA = OD \cdot x_o$, where x_o is the ratio of the distance OA between the point of minimum pressure of the equivalent yawed wing and the leading edge to the original chord OD, one obtains for the extended chord the expression

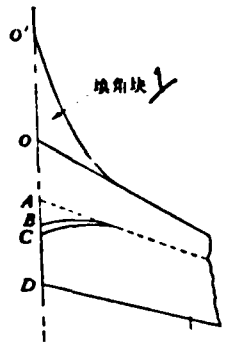

Figure 2
Key: 1--fillet

$$OD' = \frac{O'A}{x_1} = OD\left(\frac{x_0 - 1}{x_1 - 1}\right). \qquad (5)$$

To determine the spanwise shape of the leading edge of the wing root region fillet, one needs to determine the spanwise variation

of the position of the point of minimum pressure in the wing root section. Then, in accordance with the requirement that the line joining the points of minimum pressure on all the wing sections of the wing root regions should coincide with that joining the points of minimum pressure on the equivalent yawed wing, the amount of chord lengthening required for each wing section of the wing root regions can be determined in the manner described above. Thus, the shape of the leading edge of the fillet in the first approximation can be determined.

Numerical procedures are generally required for determining the pressure distribution on each wing section in the wing root regions. For the design of the shape of the fillet in the first approximation, one can employ the method suggested in [9], multiply K_3 with the first term, and K_2 with the second term on the right hand side of Equation (3), and obtain

$$C_p(x_\nu) = -\frac{2\cos\Lambda_t}{\sqrt{1-M^2\cos^2\Lambda_t}}\left[\sum_{\mu=1}^{N-1} K_3 s_{\nu\mu}^{(1)} z_\mu - K_2(\Lambda_t)\sum_{\mu=1}^{N-1} s_{\nu\mu}^{(1)} z_\mu\right] \qquad (6)$$

In the above equation, Λ_t is the sweep-back of the line joining points of constant x_ν in the wing root regions. $K_2 = 1$ at the wing root and decreases along the spanwise direction. For its values, see Figure 1 of [10]. For the values of K_3, see Equations (10) and (11) of [10].

3. ZERO-LIFT SHAPING FOR THE FUSELAGE NEAR THE WING-FUSELAGE JUNCTION FOR A GIVEN M NUMBER IN SUPERSONIC DESIGNS

After the calculations in the first approximation have been made, the pressure distribution and fuselage shaping should be computed according to the linearized supersonic theory for the three-dimensional wing. If the fuselage shaping is still too excessive, then the wing section in the wing root regions obtained in the first approximation has to be modified. The position of

maximum thickness of the wing section in the root regions should be shifted forward to beyond 15% of the chord and, if necessary, to 6.5% of the chord. The ratio of the maximum thickness of the wing section to the chord should be approximately increased so as to obtain a smooth variation along the chord for the slope of the modified new wing section. The pressure distribution and fuselage shaping should be again computed. The process is repeated until the results converge to what is desired.

For a swept-back wing-body combination, when the ratio of the wing root chord to the radius of the fuselage is greater than 6, the pressure distribution due to thickness on the wing of the combination is basically similar to those on the isolated wing obtained by regarding the side of the fuselage as a reflecting plane. Of course, there are definite differences between the two in the wing section of the root regions, especially in the rear part of the root chord. But this will not cause any appreciable error in the design [1]. Hence, one can regard the pressure distribution due to thickness on the wing obtained after fuselage shaping to be approximately equal to the sum of the pressure distribution on the wing resulting from fuselage shaping. The amount of fuselage shaping is determined from the difference between the pressure distribution due to thickness on the wing and that on the required equivalent yawed wing. Hence, one should first calculate the pressure distribution due to thickness on the isolated wing. Then calculate the pressure distribution resulting from the fuselage shaping and then calculate the amount of fuselage shaping required.

1. Calculation of pressure distributions due to thickness of the supersonic isolated wing

Consider a thin wing. The pressure coefficient due to thickness at the singular point on the wing plane ($z = 0$) has been calculated to be [11]

$$C_p(X,Y,0) = -\frac{2}{\pi}\int_{\beta_1}^{\beta_2}\int_0^{\alpha^*}\frac{(\alpha_1-\alpha)f(\alpha,\beta)d\alpha d\beta}{\bar{c}(\beta)\alpha^{1/2}(\alpha_1-\alpha_2-\alpha)^{1/2}(\alpha_1+\alpha_2-\alpha)^{1/2}}$$
$$+\frac{1}{B+\operatorname{tg}\Lambda_{01}}\left[\frac{R_0(\beta_1)}{x-sx_1^*(\beta_1)}\right]^{\frac{1}{2}}+\frac{1}{B+\operatorname{tg}\Lambda_{02}}\left[\frac{R_0(\beta_2)}{x-sx_1^*(\beta_2)}\right]^{\frac{1}{2}} \qquad (7)$$

In the above equation $(X,Y,0)$ and (α,β) denote the dimensionless quantities corresponding to the stationary point $(x,y,0)$ and the moving point (ξ,η) respectively:

$$X=\frac{x-sx_1^*(Y)}{s\bar{c}(Y)},\ Y=\frac{y}{s};\ \alpha=\frac{\xi-sx_1^*(\beta)}{s\bar{c}(\beta)},\ \beta=\frac{\eta}{s}$$

After this coordinate transformation, the front Mach line equation $\xi = x \pm B(\eta - y)$ for point (x,y,o) on the z = 0 plane becomes

$$\alpha = \alpha_1 \pm \alpha_2,\quad \alpha_1=\frac{1}{\bar{c}(\beta)}\left[X\bar{c}(Y)+x_1^*(Y)-x_1^*(\beta)\right],\ \alpha_2=\frac{B(\beta-Y)}{\bar{c}(\beta)},$$

x_1^* denotes the dimensionless quantity corresponding to the coordinate $x_1^* = x_1/s$; $\bar{c}$ denotes the dimensionless quantity corresponding to the wing section chord, $\bar{c} = c/s$; s denotes the half-span of the wing; $R_0(\beta_1)$ and $R_0(\beta_2)$ denote the radius of the wing leading edge at β_1 and β_2, respectively; Λ_{01} and Λ_{02} denote the sweep-back of the wing leading edge at β_1 and β_2, respectively, where β_1 is the β coordinate of the point of intersection of the right front Mach line $\alpha = \alpha_1 - \alpha_2$ of the fixed point (x,y,o) and the right leading edge, and β_2 is the β coordinate of the point of intersection of the left front Mach line $\alpha = \alpha_1 + \alpha_2$ of the fixed point (x,y,o) and the left leading edge; $f(\alpha,\beta)$ is the wing surface slope function at point (α,β), $f(\alpha,\beta)=\frac{\partial z(\xi,\eta)}{\partial\xi}\alpha^{\frac{1}{2}}$; $B=\sqrt{M^2-1}$.

For a subsonic leading edge and a supersonic trailing edge, the domain of integration for Equation (7) can be divided into three regions, as shown in Figure 3. For region (1), $\alpha^* = \alpha_1 - \alpha_2$; for regions (2) and (5), $\alpha^* = \alpha_1 + \alpha_2$. Thus Equation (7) can be rewritten as

$$C_p = \frac{2}{\pi}\left[-\int_y^{\beta_1}\int_0^{\alpha_1-\alpha_2} A\,d\alpha\,d\beta - \int_0^{Y}\int_0^{\alpha_1+\alpha_2} A\,d\alpha\,d\beta - \int_{\beta_2}^{0}\int_0^{\alpha_1+\alpha_2} A\,d\alpha\,d\beta\right]$$
$$+ \frac{1}{B+\operatorname{tg}\Lambda_{01}}\left[\frac{R_0(\beta_1)}{x - sx_1^*(\beta_1)}\right]^{\frac{1}{4}} + \frac{1}{B+\operatorname{tg}\Lambda_{02}}\left[\frac{R_0(\beta_2)}{x - sx_1^*(\beta_2)}\right]^{\frac{1}{4}} \qquad (8)$$

in which $A = \frac{(\alpha_1-\alpha)f(\alpha,\beta)}{c(\beta)\alpha^{1/2}(\alpha_1-\alpha_2-\alpha)^{1/2}(\alpha_1+\alpha_2-\alpha)^{1/2}}$, and $\int$ denotes the finite portion of the integral.

As the integrand A in Equation (8) contains a singularity at $\alpha = 0$ (leading edge) and another one at $\alpha = \alpha_1 + \alpha_2$ (on the front Mach line), these singularities have to be removed before numerical integration can be performed. For integrals containing square-root singularities, such as

$$\int_0^{\alpha_1-\alpha_2} \frac{d\alpha}{\alpha^{1/2}(\alpha_1-\alpha_2-\alpha)^{1/2}},$$

we can make the following variable substitution:
Let $\alpha = 0.25(\alpha_1-\alpha_2)(1+\zeta)^2(2-\zeta)$, . The integral then becomes $\int_{-1}^{1}\frac{3d\zeta}{(4-\zeta^2)^{1/2}}$, in which the integrand is positive everywhere with the range of integration. After this treatment, no more singularities exist in the integrals in Equation (8) and the Gaussian method can be applied in the numerical integration.

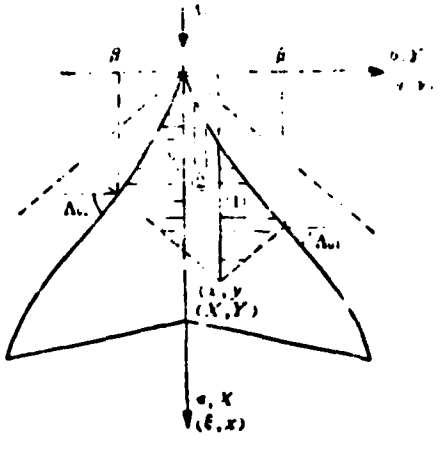

Figure 3

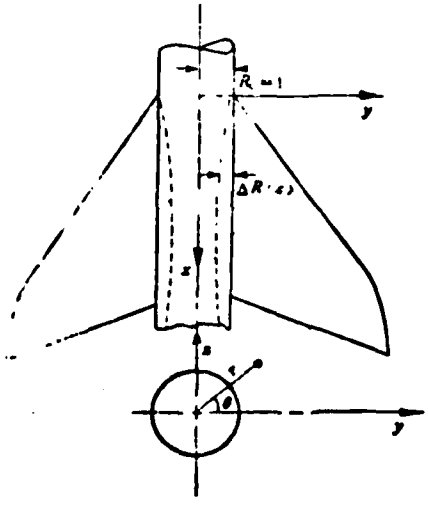

Figure 4

2. Pressure distribution on wing and fuselage caused by symmetrical fuselage shaping in supersonic flow fields

Let the equation for symmetrical fuselage shaping be

$$\frac{\partial R}{\partial x} = t \sum_{n=0}^{\infty} g_{2n}(x) \cos 2n\theta \tag{9}$$

For a mid-wing arrangement, the pressure distribution on the wing and the fuselage caused by symmetrical fuselage shaping is given by [12,13]. (Let $B=\sqrt{M^2-1}$)

$$C_{p,n}(x) = \frac{2t}{B} \sum_{n=0}^{\infty} \cos 2n\theta \left[g_{2n}(x) - \frac{1}{B} \int_0^x g_{2n}(\xi) W_{2n}\left(\frac{x-\xi}{B}, 1, \xi\right) d\xi \right] \tag{10}$$

$$C_{p,n}(x) = \frac{2t}{B} \sum_{n=0}^{\infty} \left[\frac{g_{2n}(x - Br + B)}{\sqrt{r}} - \frac{1}{B} \int_0^{x-Br+B} g_{2n}(\xi)\, W_{2n}\left(\frac{x}{B} - r + 1 - \frac{\xi}{B}, r\right) d\xi \right] \tag{11}$$

In the above equations, all the lengths have been divided by the radius R_o of the cylindrical section of the unwaisted fuselage; the x-axis lies along the axis of the fuselage, the y-axis passes through the point where waisting begins and (x,r,θ) form a cylindrical coordinate system (see Figure 4); R is the radius of the fuselage after waisting; t is a specific parameter, usually taken as the relative thickness of the wing root wing section; g_{2n} is the amplitude of fuselage shaping; W_{2n} is the set of special functions associated with the boundary value problem of solving the wave equation;see [14]. For a symmetrical fuselage, we may set n = 0 in Equations (10), (11). Then setting r = 1 will give the pressure distribution on the wing root wing section produced by the fuselage shaping.

Non-midwing arrangement is an important measure for reducing fuselage shaping. We have in [5] found the additional pressure

distribution on the wing root wing section due to the non-midwing arrangement in the case of axially symmetrical fuselage shaping to be

$$\Delta C_{p_1}(x) = -\frac{1}{\pi}\left\{F\frac{d^2R}{dx^2} + N\frac{dR}{dx}\right\} = -\frac{t}{\pi}\left\{F\frac{d}{dx}\left(\frac{dR}{dx}\right) + N\left(\frac{dR}{dx}\right)\right\} \qquad (12)$$

See Equation (39) in [5] for the definition of the functions F and N. Hence, the pressure distribution produced by axially symmetric fuselage shaping on the wing root wing section in a non-midwing arrangement will be given by

$$C_{p_{1+2}}(x) = C_{p_{2+2}}(x) + \Delta C_{p_1}(x) = \frac{2t}{B}\left[g_0(x) - \frac{1}{B}\int_0^x g_0(\xi)W_0\left(\frac{x-\xi}{B},1\right)d\xi\right] - \frac{t}{\pi}\left[F\frac{dg_0}{dx} + Ng_0\right] \qquad (13)$$

Key: 1--non-midwing; 2--midwing

3. The design of fuselage shaping near the junction of the wing and fuselage

If the required pressure distribution on the wing root wing section is $C_{p_1}(x)$, the wing root wing section pressure distribution for unwaisted fuselage is $C_{p_2}(x)$, and the pressure distribution on the cylindrical section of the fuselage due to the effect of the forebody is $C_{p_3}(x)$, , then we require that the pressure distribution after axially symmetric fuselage shaping be $C_p(x) = C_{p_1}(x) - C_{p_2}(x) - C_{p_3}(x)$. For a non-midwing arrangement, this is just the value of C_p on the left hand side of Equation (13) and Equation (13) is an integral equation involving $g_0(x)$ which can be solved by numerical integration using the trapezoidal formula. If we take the interval to be δ, then when $x = m\delta$, by setting $\left(\frac{dg_0(x)}{dx}\right)_{x=m\delta} = \frac{g_0(m\delta) - g_0(\overline{m-1}\delta)}{\delta}$, one obtains from Equation (13)

$$g_0(m\delta) = \left[\frac{B}{2t} C_p(m\delta) + \frac{\delta}{B}\left\{\frac{1}{2} g_0(0) W_0\left(\frac{m\delta}{B}, 1\right) + \cdots + g_0(\overline{m-1}\delta) W_0\left(\frac{\delta}{B}, 1\right)\right\} - \frac{B}{2\pi\delta} F g(\overline{m-1}\delta)\right] \Big/ \left[1 - \frac{\delta}{2B} W_0(0, 1) - \frac{B}{2\pi\delta}(F + N\delta)\right] \tag{14}$$

In the above equation, $g_0(0)$ can be determined from Equation (13) to be

$$g_0(0) = C_p(0) \Big/ t\left(\frac{2}{B} - \frac{N}{\pi}\right) \tag{15}$$

In the case of a midwing arrangement, let F = N = 0 in Equations (14) and (15). After obtaining the value for $g_0(m\delta)$, we integrate Equation (9) for the condition that n = 0 by means of the trapezoidal formula by an approximation and obtain the radius of the waisted fuselage.

$$\begin{aligned} R(m\delta) &= 1 + t\int_0^{x=m\delta} g_0(\xi) d\xi \\ &= 1 + t\delta\left\{\frac{1}{2}[g_0(0) + g_0(m\delta)] + g_0(\delta) + g_0(2\delta) + \cdots + g_0(\overline{m-1}\delta)\right\} \end{aligned} \tag{16}$$

If we require that the fuselage be smooth where the wing-fuselage junction commences, i.e., that $\left.\frac{\partial R}{\partial x}\right|_{x=0} = g_0(0) = 0$, then we see from Equation (15) that we must have $C_p(0) = 0$ at x = 0. If, in addition, we require the axial cross-section area distribution satisfy the "area rule", then the fuselage shaping will not be axially symmetric. Assume the fuselage shaping equation to be

$$\frac{\partial R}{\partial x} = t\sum_{n=0}^{1} g_{2n}(x)\cos 2n\theta \tag{17}$$

and the area distribution demanded by "area rule" to be S(x). Then (see Figure 5).

From Equation (18) one obtains

$$g_0(x) = \frac{1}{2\pi t}\frac{dS}{dx} = M(x) \tag{19}$$

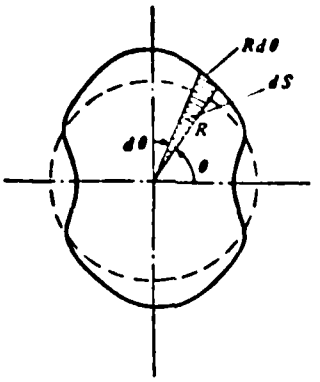

Figure 5

$$S(x) = \int_0^{2\pi} \frac{1}{2} R \cdot R d\theta = \frac{1}{2}\int_0^{2\pi} R^2 d\theta$$

$$\frac{dS}{dx} = \int_0^{2\pi} R \frac{\partial R}{\partial x} d\theta = \int_0^{2\pi} [1 + O(t)] \frac{\partial R}{\partial x} d\theta$$

$$= t \sum_{n=0}^{1} g_{2n}(x) \int_0^{2\pi} \cos 2n\theta d\theta + O(t^2) = 2\pi t g_0(x) + O(t^2) \qquad (18)$$

Suppose the pressure distribution produced by fuselage shaping as required by the wing root wing section is $t(C_{po}(x)$; then from Equations (11) and (12), we obtain (considering that ΔC_p is approximately also applicable in the axially symmetrical case)

$$tC_{p_0}(x) = \frac{2t}{B}\left[g_0(x) - \frac{1}{B}\int_0^x g_0(\xi) W_0\left(\frac{x-\xi}{B}, 1\right) d\xi + g_2(x) \right.$$
$$\left. - \frac{1}{B}\int_0^x g_2(\xi) W_2\left(\frac{x-\xi}{B}, 1\right) d\xi \right] - \frac{t}{\pi}\left\{ F \frac{dg_0}{dx} + N g_0 \right\} \qquad (20)$$

Substituting Equation (19) into the above equation, one obtains

$$g_2(x) - \frac{1}{B}\int_0^x g_2(\xi) W_2\left(\frac{x-\xi}{B}, 1\right) d\xi = \frac{B}{2} C_{p_0}(x) - M(x)$$
$$+ \frac{1}{B}\int_0^x M(\xi) W_0\left(\frac{x-\xi}{B}, 1\right) d\xi + \frac{B}{2\pi}\left\{ F \frac{dM}{dx} + NM(x) \right\} - P_2(x) \qquad (21)$$

in which we let

$$P_2(x) = \frac{B}{2} C_{p_0}(x) - M(x) + \frac{1}{B}\int_0^x M(\xi) W_0\left(\frac{x-\xi}{B}, 1\right) d\xi$$
$$+ \frac{B}{2\pi}\left\{ F \frac{dM}{dx} + NM(x) \right\} \qquad (22)$$

The integrals in Equations (21) and (22) can be computed by approximate integration using the trapezoidal formula. After substituting $S_0(x)$ from Equation (19) and $S_2(x)$ determined from Equation (21) into Equation (17), one can obtain the amount of fuselage shaping $\Delta R(x,\theta)$ at different positions x,θ. For the case of a midwing arrangement, let N = F = 0 in each of the above equations.

Finally, the fuselage shaping at the wing-fuselage junction must be such that it smoothly connects to the fuselage shaped according to the "area rule" behind the trailing edge of the wing root wing section.

The results of computation for actual examples show that for a given reduction in zero-lift drag, the amount of shaping is smaller for a lower isolated wing arrangement and is smaller than that required for a midwing arrangement. This is easy to comprehend as, in the non-midwing arrangement, the shielding effect of the fuselage on the upper surface of the wing is enhanced, thus augmenting the effect of the fuselage shaping. Hence, non-midwing arrangement is an important measure for reducing the amount of fuselage shaping.

REFERENCES

[1] Lock, R. C. & Bridgewater, J., Theory of aerodynamic design for swept-winged aircraft at transonic and supersonic speeds, Progress in Aeronautical Sciences, 8, Pergamon Press (1967).

[2] Lock, R. C., *Aero. Quart.*, 12 (1961).

[3] Bridgewater, J., Lock, R. C., Theoretical and experimental investigation of wing-body configurations at low supersonic speeds, AGARD-CP71-71 (1971).

[4] Bridgewater, J. & Wilson, K. H., Influence of wing root shaping on the pressure distribution of swept-wing body configurations, A. R. C.—CP1109 (1970).

[5] Chu Hang, Li Hsüeh, 3(1979), 182-190.

[6] Kuchemann, D., *J. R. A. S.*, 61 (1957).
[7] Weber, J., The calculation of the pressure distribution over the surface of two dimensional and swept wings with symmetrical aerofoil sections, A. R. C. —— R & M 2918.
[8] Kuchemann, D. & Weber, J., The subsonic flow pass swept wings at zero lift without & with body, A. R. C. —— R & M 2908.

[9] Haines, A. B., *J. R. A. S.*, 61 (1957).
[10] Method for predicting the pressure distribution on swept wings with subsonic attached flow. Royal Aeronautical Society Transonic Data Memorandum 6312.
[11] Eldrige, R. H., A numerical method for calculating the pressure due to thickness on symmetrical wings at zero incidence in supersonic flow, A. R. C. —— R & M 3535 (1966).
[12] Nilsen, J. N., Quasi-cylindrical theory of wing-body interference at supersonic speeds and comparison with experiments, NACA-TR1252.
[13] Jones, J. G., A method for designing body shape to produce prescribed pressure distribution on wing body combinations at supersonic speeds, A. R. C. —— CP 540.
[14] Nilsen, J. N., Tables of characteristic functions for solving boundary value problems of the wave equation with application to supersonic interference, NACA —— TN 3873.

THE WAVE DIAGRAMS FOR DIFFRACTION AND REFLECTION OF A TRAVELING WEAK SHOCK WAVE FROM AN OPEN END OF A SHOCK TUBE

Wei Chung Lei, Wang Ping-cheng, Chang Chün Hsiu
(Tsi Ching University)

Abstract

The free diffractions of a weak shock wave issuing from an open end of a shock tube and the formation and development of a vortex ring from the end of the tube are observed by a schlieren method. Also observed are the oblique reflections from the horizontal floor and the vertical plate.

As the wave described above impinges on the horrizontal surface near grazing incidence, the Mach stem forms. Under certain conditions, when this Mach stem travells along a slant surface with an incidence angle which is larger than the critical value with respect to the horrizontal axis, the phenomena of "dissolution" of the Mach stem occurs.

The observation of such a new phenomena and its analysis are presented in this paper.

In 1971, we used a Schlieren method to study the flow diagrams of a weak shock wave emitted from a shock tube and the induced ultra-pressure field. The shock wave inside the tube is planar and the gas flow velocity in the wake of the wave is in the subsonic range. After issuing from the opening of the shock tube, the wave itself is diffracted and undergoes regular reflections from the horizontal floor and the vertical plate. At the same time, the gas flow in the wake of the wave forms a vortex ring outside the tube which travels forward at a definite velocity. In addition, a sonic emitted flow field is formed near the open end of the tube. When this shock wave travels along a slanted surface, one further observes the so-called "dissolution" phenomenon in which the incident wave and the reflected wave travel separately along the slanted surface. Such "dissolution" is a new phenomenon which we will describe and explain on a physical basis in this paper. Observations have been made on the flow diagrams of waves issuing from both porous and nonporous tube walls.

1. WAVE DIAGRAMS

After the weak shock wave issues from the open end of the shock tube, it is first diffracted. The corner of the open end of the tube can be regarded as a source of interfering waves. Hence, the shock wave will be attenuated by these interfering waves, and its wavefront changes from a planar to an ellipsoidal shape when it has traveled a distance equal to the distance of the tube (plate I, photo 1).

The main shock wave undergoes regular oblique reflection from the horizontal floor. Under our experimental conditions, one can calculate the variation of the intensity of the shock wave with distance from the tube opening by measuring the angles of incidence and reflection (plate I, photo 2). One should note that, although the reflection from the floor is an oblique reflection, its destructive effect is not negligible. Roughly speaking, for medium strong shock waves, the ultra-pressure in the wake of the reflected wave is on the same order of magnitude as that of the main reflected wave. For weak shock waves, it could even exceed the latter.

For reflection of the shock wave from a vertical plate placed at a distance equal to twice the diameter of the tube, the relation between the angles of incidence and reflection is, on the whole, that for regular reflection (plate I, photo 3). After the shock wave is reflected, it suffers from the disturbance from the vortex ring and the emitted gas flow and is no longer a spherical wave. Rather, it becomes bow-shaped in the two-dimensional case, and saucer-shaped in the three-dimensional case. After it passes through the vortex ring, the main reflected wave increases the pressure in the original flow region. In the case of a porous wall, the reflected wave is still saucer-shaped.

In the process of backward movement along the floor of the incident wave reflected off the vertical plate and the reflected wave, Mach reflection is sure to occur. The height of the Mach stem of this Mach reflection (i.e., the height of the fork) increases as the wave moves on, and the intensity of the Mach wave gradually decreases. Therefore, under the conditions of given incident wave intensity and given angle of incidence, the height of the Mach stem can be qualitatively used as a basis for estimating the attenuation of the Mach wave. Under our experimental conditions, the position of this fork rises with a slope of approximately 15°. The wave diagram for reflection off the vertical plate is shown in plate I, photos 4 and 5.

For the case where the vertical plate is placed at a distance equal to twice or four times the tube diameter, the reflection near the tube is a Mach reflection whether the wall is porous or not. Experimental results show that, under these conditions, the destructive effects of the reflected wave on the obstacles and structures in the vicinity of the wall is obviously larger than that of the diffracted main shock wave.

2. THE EMITTED GAS FLOW AT THE OPENING OF THE TUBE

Two cases need to be considered for the emitted gas flow, viz. the case where the flow after the shock wave in the tube is subsonic and the case where it is supersonic.

For the case where the gas flow at the cross-section of the tube opening is initially subsonic, generally speaking, before the vortex ring leaves the end of the tube, the divergent waves arising at the corner of the tube opening will be transmitted into the tube. This results in increased velocity of the gas flow at the cross-section of the tube opening, which eventually becomes sonic. The wavefront of the above mentioned divergent waves have a stronger thinning effect.

The emitted gas flow following the main shock wave gradually develops from the unaffected trumpet-shaped region into the peach-shaped region as a result of the thinning effect of the divergent waves. This peach-shaped region is where the two divergent waves arising from the corner of the tube opening interfere. It should be pointed out that despite the fact that the main shock wave is continually impinged upon by the divergent waves, as the gas flow emitted from inside the tube keeps on replenishing energy, the ultra-pressure of the shock wave in the vicinity of the central region of the gas flow is actually larger than that in the regions above and below. This is characteristic of the diffraction of the shock wave after issuing from the tube opening.

After the gas flow at the cross-section of the tube opening has been accelerated to sonic velocity by the divergent waves, as the pressure at the tube opening is higher than that outside the tube, the gas flow will continue to be accelerated beyond the tube opening, forming a local supersonic flow region at the tube opening (plate I, photo 6, plate II, photo 7). When the ultra-pressure of emission is 1 kg/cm^2, the Mach number measured for the local supersonic flow for a tube with a nonporous wall is 1.18; while that for a tube with a porous wall is 1.05. Therefore, the Mach number decreases approximately by 11% when the wall is porous.

For the case where the gas flow at the cross-section of the tube opening is supersonic, supersonic emitted flow is formed at the corner of the opening and the divergent waves from the corner will not be able to enter the tube. As the pressure at the tube opening is larger than the atmospheric pressure of the surrounding, the free boundary of the gas flow will certainly expand outward. The flow diagram is similar to that for the stable, constant supersonic emitted flow.

3. THE FORMATION, DEVELOPMENT AND SHATTERING OF THE VORTEX RING

Because of the effect of adhesion, when the gas flows around a pointed corner, a small kernel of vortex ring with a diameter just a little larger than the inner diameter of the tube, is first formed close to the end of the tube. As time goes on, the gas behind the main shock wave keeps feeding the vortex ring. The vortex ring grows fatter and fatter until it finally leaves the tube opening and travels forward at a definite velocity. Because the vortex ring undergoes turbular flow diffusion and momentum exchange with the surrounding gas flow, it further increases in diameter and fatness. However, as a result, the vortex ring becomes looser and looser until it finally falls apart.

After the vortex ring leaves the tube end, it is first accelerated. The velocity reaches a maximum when it has traveled a distance approximately twice the tube diameter. What follows is decelerated motion, shattering and dissipation.

For shock waves driven by high pressure compressed air in a nonporous tube, when the ultra-pressure of emission is 1 kg/cm^2, the average velocity of the vortex ring is 127 m/s; when the ultra-pressure is 4 kg/cm^2, the average velocity of the vortex ring is 156 m/s. For shock waves driven by explosive gas, when the ultra-pressure of emission is 15 kg/cm^2, the average velocity of the vortex ring is 129 m/s.

For shock waves driven by high pressure compressed air in a porous tube, because the emitted shock wave is attenuated, the velocity of the vortex ring is lower by about 10%. In the case of the nonporous tube, the time elapsed before the vortex ring leaves the tube opening is about 250 μs. In the case of the porous tube, the vortex ring leaves the tube opening earlier by about 8%.

4. FLOW DIAGRAM NEAR A POROUS WALL AND THE DISSIPATING EFFECT OF THE PORES

After the main shock wave passes through the pores in the wall, it is emitted out of the pores and diffracted. The waves leaking out of the pores diffuse rapidly and their intensity is rapidly attenuated. At the same time, these waves superpose on one another and form a Mach cone envelope with finite amplitude (plate II, photo 8). The oblique reflection from the floor and the vertical plate of the main diffracted wave has similar wave diagrams for porous and nonporous walls (plate II, photo 9). The pore content of the porous walls discussed in this paper is 1.44% or 2.78%. The pores are uniformly distributed.

What comes after the main shock wave in the tube is a high pressure gas flow. Under the action of this high pressure gas flow the gas particles will certainly be emitted through these small pores into the stationary gas outside of the tube. Hence, a small emitted flow is formed at each pore. When the shock wave is barely emitted from the tube opening, the emitted flow field near the pores has already formed. Approximately at the time the vortex ring is at a distance equal to 1.5 times the tube diameter from the tube opening, owing to the adhesion effect of the gas, the turbular flow diffusion and momentum exchange among the gas particles in the center region of the emitted flow and those in the surrounding stationary gas result in the merging of the small emitted flow fields at their outer edges.

When the reflected shock wave passes through the emitted flow region at the tube opening and the emitted flow region near the pores, the shock wave will develop two wavefronts (plate II, photo 10).

The waves escaping from the pores can be nothing more than waves with finite amplitudes. It is thus completely reasonable to

assume that these spread out at sonic speeds. Hence, we can deduce the intensity of emission of the main shock wave at the tube opening from the angle of the Mach cone of the envelope of the waves escaping through the pores. The shock wave intensity obtained this way agrees fairly well with that measured with other methods.

The analysis given in Section 1, 2 and 3 shows that the pores in the tube wall can indeed reduce the intensity of the emitted shock wave. Experimental results show that the intensity of the emitted shock wave is less for porous walls than for nonporous walls by about 16% (at the tube opening) and 9% (at a distance 1.8 times the tube diameter from the opening). Qualitatively speaking, we consider the drop to be about 10%.

5. OBSERVATION OF A WEAK SHOCK WAVE TRAVELING ALONG A SLANTED SURFACE USING OPTICAL METHODS AND ITS ANALYSIS

When the shock wave emitted from the end of the tube and the wave reflected off the floor travel together along a slanted surface, the flow diagrams and the formation of the wave system is very complicated. First, the incident shock wave and the wave reflected off the floor are not planar but are curved. Next, before they hit the slanted surface, they have already formed Mach reflection but with a rather short Mach stem. Furthermore, after they hit the slanted surface, the interfering wave arising from the corner first impinges on the Mach stem and the original reflected wave. In general, after the Mach stem hits the slanted surface at a definite angle of incidence, reflection of the Mach stem is expected to occur. However, we found in our experiments that in the actual flows the Mach stem "dissolved" and reflection of the original incident wave and that of the wave reflected off the floor occurred separately. This is evident in many of the pictures taken (plate III, photos 13-20).

Now let us explain this phenomenon. First, we analyze the wave diagrams for the case where the Mach stem has been formed before the weak shock wave hits the slanted surface. This is the case for the 30° and 45° slants.

Right after the shock wave hits the corner of the slanted surface, the disturbance of the corner results in the formation of a series of compression waves. As the gas flow behind the shock wave is always subsonic relative to the shock wave, the compression waves will keep impinging on the shock wave. The wavefront of these compression waves is the fan-shaped arc in the photos. As the shock wave is very weak, the reflected wave of the Mach stem merges with the wavefront of the compression waves. Note that the formation and growth of the Mach stem in the Mach reflection is always caused by the incident wave being pushed from the back by the oblique reflected wave. In our case, the slope of rise of this Mach stem is about 15°. Hence, the process of traveling along the 30° and 45° slants is simply the process of reflection of the Mach stem from the slanted surface and that of the shortening of the Mach stem. Those parts of the entire wave (the original incident and reflected waves) that have not been disturbed or reflected by the slanted surface or the corner will continue traveling in the original direction at the original speed. As the waves progress along the slanted surface, the Mach stem is gradually shortened and eventually the fork meets the slanted surface. What follows is the individual reflection and shortening of Mach stem of the incident and reflected waves. The reflected wave of the original wave is tangent to the wavefront of the compression waves issuing from the corner; the reflected wave of the original reflected wave, on the other hand, merges with the wavefront of the compression waves. This is how the Mach stem is "dissolved" and how the original incident and reflected waves separate to be independently reflected and to travel separately along the slanted surface.

[Plate III, photos 13-15 (30° slant); Plate III, photos 16-18 (45° slant)]

For the wave diagrams in which the Mach stem has not been formed before the incident shock wave hits the slanted surface, the process of traveling along the slanted surface is the same as the foregoing, i.e., one in which the incident wave and the reflected wave are separated (plate IV, photos 19-20 (60° slant)). However, for a 15° slant, as the slope of the slanted surface is about the same as that of the rise and growth of the Mach stem, the incident wave and the reflected wave do not separate in the process of traveling along the slanted surface. Here one only observes the impingement of the compression waves on the original shock wave (plate II, photos 11,12).

Thus we see that the wave diagrams for the weak shock wave traveling along a slanted surface depends on the intensity of the wave, the slope of rise of the Mach stem and the fork and also on the slope of the slant itself. To obtain the detailed quantitative relationship among these factors, one needs to make further experimental observations and perform the corresponding numerical calculations.

We are thankful for the assitance and support given to us by Comrades Lu Shih Chia and Wang Ju Chih. Other participants of this project include Comrades Liu K'e Ch'i, Li Ch'ang Ling and Huang Wen Sheng.

END

DATE
FILMED
10-81

DTIC